INL/EXT-17-42714
Revision 0

BWR Full Fuel Assembly Testing and Validation

Su-Jong Yoon
Emilio Baglietto
Giulia Agostinelli

August 2017

The INL is a U.S. Department of Energy National Laboratory
operated by Battelle Energy Alliance

INL/EXT-17-42714
Revision 0

BWR Full Fuel Assembly Testing and Validation (L3 Milestone THM.CLS.P15.10)

Su-Jong Yoon[1]
Emilio Baglietto[2]
Giulia Agostinelli[2]

[1]Idaho National Laboratory
[2] Massachusetts Institute of Technology

August 2017

Idaho National Laboratory
Idaho Falls, Idaho 83415

http://www.inl.gov

Prepared by
IDAHO NATIONAL LABORATORY
Idaho falls, ID 83415
for the
U.S. DEPARTMENT OF ENERGY
under contract DE-AC05-00OR22725

(This page intentionally left blank)

BWR Full Fuel Assembly Testing and Validation
(L3 Milestone THM.CLS.P15.10)

Su-Jong Yoon
Department of Fusion, Hydrogen and Measurement Sciences
Nuclear Science and Technology Division
Idaho National Laboratory
2525 Fremont Ave. Idaho Falls, ID 83415

Emilio Baglietto and Giulia Agostinelli
Department of Nuclear Science and Engineering
Massachusetts Institute of Technology
77 Massachusetts Ave. Cambridge, MA 02139

EXECUTIVE SUMMARY

This report describes the Consortium for Advanced Simulation of Light Water Reactors (CASL) work conducted for completion of the Thermal Hydraulics Methods (THM) Level 3 milestone THM.CLS.P15.10: BWR Full Fuel Assembly Testing and Validation.

The extension of existing boiling closure designed for Pressurized Water Reactors (PWRs) to the high void fraction condition of Boiling Water Reactors (BWRs) is one of the challenges for Multiphase Computational Fluid Dynamics (M-CFD) applications. In the efforts aimed at developing the advanced boiling closure for BWRs, the baseline closure model, so-called 'Zero' closure, has been developed based on the GEN-I closure for PWRs. This baseline closure model is physic-based, simplest and robust, but it does not contain any explicit descriptions of the complex high void fraction mechanisms. Therefore, its applicability needs to be evaluated for further development of advanced CASL-BWR closures. In order to support this need, the high fidelity M-CFD simulation with the Zero closure has been conducted for BWR full fuel assembly. The capabilities of M-CFD with the Zero closure were evaluated against the international OECD/NRC BFBT benchmark data. The scalability of M-CFD application to the nuclear fuel assembly was investigated by utilizing the High Performance Computing (HPC) system at the Idaho National Laboratory (INL). This report also presents the recent view of the best practices on the M-CFD for BWRs to provide a useful reference to identify and overcome common challenges in the M-CFD applications.

(This page intentionally left blank)

ACKNOWLEDGEMENTS

This research was supported by the Consortium for Advanced Simulation of Light Water Reactor (www.casl.gov), an Energy Innovation hub (http://www.energy.gov/hubs) for Modeling and Simulation of Nuclear Reactors under U.S. Department of Energy Contract No. DE-AC05-00OR22725.

(This page intentionally left blank)

CONTENTS

TABLES

FIGURES

NOMENCLATURE

A_D	Mean linearized drag coefficient
a_{ij}	Interfacial area density
C	Cost of parallel computation
C_D	Drag Coefficient
c_p	Specific heat
D_b	Bubble diameter
d_w	Bubble departure diameter
E	Total energy
F	Interfacial forces
f	Bubble departure frequency or
f_D	Drag correction factor
$\mathbf{F}_{int}$	Internal forces
$\mathbf{f}$	Body force vector
$\mathbf{g}$	Gravity vector
H	Total enthalpy
$h_i(T_{ij})$	Phase i enthalpy at interface temperature T_{ij}
h_{lg}	Latent heat of fluid
h	Heat transfer coefficient
k	Thermal conductivity
K_{dry}	Wall dryout area fraction
K_{quench}	Quenching influence wall area fraction
$\mathbf{M}_i$	Interphase momentum transfer
$\dot{m}_{ij}$	Mass transfer rate to phase i from phase j
$\dot{m}_{ji}$	Mass transfer rate to phase j from phase i
n''	Nucleation site density
p	Pressure
Q	Interphase heat transfer rate
$\dot{q}''_{conv}$	Convective heat flux
$\dot{q}''_{dry}$	Vapor contribution to convective heat flux
$\dot{q}''_{evap}$	Evaporative heat flux at wall
$\dot{q}''_{quench}$	Quenching heat flux
S	Speedup factor
S_{k_c}	Turbulent kinematic energy source term
S_{ε_c}	Turbulent dissipation source term
S_i^{α}	Phase mass source term
S_i^{v}	Phase momentum source term
$S_{u,i}$	Energy source term
T	Temperature
$\mathbf{T}_i$	Viscous stress tensor
t_w	Waiting time
$\mathbf{v}$	Velocity vector
y_w	Distance from the wall to the bubble
α	Volume fraction
α_{dry}	Wall dryout break-point
ν_c^t	Liquid phase turbulent kinematic viscosity
ρ	Density
ς	Parallelizable fraction
σ_α	Turbulent dispersion Prandtl number
τ_i	Molecular stress
τ_i^t	Turbulent stresses
χ	Void fraction

Subscripts

D	Drag force
eff	Effective
g	Vapor phase
L	Lift force
l	Liquid phase
$quench$	Quenching
TD	Turbulent dispersion force
VM	Virtual mass force
w	Wall
WL	Wall lubrication force

1. MILESTONE DESCRIPTION

The objectives of this milestone is to evaluate the applicability, robustness and performance of the baseline zero closure and Multiphase Computational Fluid Dynamics (M-CFD) for Boiling Water Reactor (BWR) applications implemented in the Consortium for Advanced Simulation of Light Water Reactors (CASL) CFD code.

High fidelity M-CFD modeling is a complex research area that relies on the validity of its mechanistic closures. While extensive effort is being devoted to evaluate and improve the closure validity and predictive capabilities, as part of the CASL effort, the heat and mass transfer characteristics in two-phase flow boiling still remain challenging. For instance, the extension of existing boiling closures to the high void fraction conditions of BWRs is still an open issue. The scales that need to be resolved vary widely from the millimeter scale of the multiphase structures to the meters scale of the core geometry. This multi-scale problem requires extremely high computational effort in order to avoid geometric simplifications that would introduce large uncertainty in the computational result. In the M-CFD simulations, which are most commonly based on efficient second order accurate finite volume solution methods, the mesh structure and quality have an observable influence not only on the accuracy of result but also on the robustness of the simulation. While automated unstructured mesh generation, e.g. trimmed mesh, tetrahedral mesh and polyhedral mesh, etc., are desirable from an application viewpoint, control of the mesh quality is not always optimal, or straightforward. Furthermore, the high performance computing capability is a promising solution for M-CFD for nuclear reactor fuel assemblies, but the scalability of parallelization still needs to be assessed and optimized. The physical modeling and computational challenges make CFD simulations of BWR fuel assemblies an important challenge for the industry. Series of studies [1, 2, 3, 4, 5, and 6] have being performed to develop and validate the CFD models for the simulations of two-phase flow phenomena in BWR core.

The Eulerian M-CFD model with a baseline boiling closure, which is so called ‘zero closure’, has been developed leveraging the experience gained through the Numerical Nuclear Reactor project [3] for BWR applications. Since this baseline model does not contain any explicit descriptions of the complex high void fraction mechanisms, the term ‘zero’ was used to identify this simplest model possible on which future Generation 1 and Generation 2 models for BWR will be built. In the BWRs, the coolant flow at the bottom starts from low void fraction. Thus, the GEN-I boiling closure designed for PWR applications was used as a starting point of BWR boiling closure. The assessments of zero closure and M-CFD applicability will provide the reference data for further development of BWR boiling closures. In this milestone, the Eulerian-Eulerian M-CFD model with the zero closure has been implemented to the CASL CFD tool, *STAR-CCM+*, and its capabilities for BWR fuel assemblies evaluated against the international OECD/NRC BWR Full-size Fine-mesh Bundle Test (BFBT) benchmark data [7]. The BFBT benchmark provides unique high-resolution void fraction measurements for a wide variety of flow conditions and void fraction values, and allows assessing the accuracy of thermal-hydraulic models for two-phase flows in BWR geometries. This report provides a recent view at best practices for CFD simulation of BWR fuel assemblies that can provide a useful reference to identify and overcome common challenges in the application of multiphase CFD tools. The milestone required completion of the following tasks:

- Construct a full detail computational fluid dynamics (CFD) model
- Describe and implement the BWR baseline zero closure
- Assess the applicability of M-CFD with the baseline zero closure
- Identify the current best practices for M-CFD simulation
- Submission of this report

2. BASELINE ZERO CLOSURE

The zero closure is the baseline boiling closure model for BWR application that aims at a simple and robust representation of the key mechanisms of the physics of the two-phase flow, rather than aiming at the absolute accuracy of the predictions, as a consequence of the still limited high grade CFD experiments available to improve and validate the separate mechanisms. This model has been developed based on the standard Generation-I boiling closure model for Pressurized Water Reactor (PWR) [8]. In the zero closure, the three-field approach was employed to calculate the interaction length scale while the Kurul-Podowski correlation [9] was used in the standard PWR GEN-I model. The three fields of the bubbly flow, intermediate flow and annular flow regimes are determined by the void fraction. The lift force term of the baseline boiling closure was modeled leveraging the previous re-evaluation result of the lift force [10]. Tomiyama correlation [11] for drag coefficient was employed as Lo & Osman suggested [12] instead of Schiller-Naumann correlation [13]. Interfacial area density was calculated by assuming the spherical bubbles. Chen-Mayinger [14] correlation was used to model the condensation of fluid. The details of the baseline zero closure are described in Section 2.2.

2.1 Transport Equations

The Eulerian-Eulerian (two-fluid) formulation of the CASL CFD tool, *STAR-CCM+ v11.04.010-R8,* is employed as the M-CFD framework. Detailed descriptions of governing equations can be found in [15] and [16].

Mass conservation:

$$\frac{\partial}{\partial t}\int_V \alpha_i \rho_i \chi \, dV + \oint_A \alpha_i \rho_i \chi \left(\mathrm{v}_i - \mathrm{v}_g\right)\cdot d\mathrm{a} = \int_V \sum_{j\neq i}\left(\dot{m}_{ij} - \dot{m}_{ji}\right)\chi \, dV + \int_V S_i^{\alpha} dV \tag{1}$$

$$\sum_i \alpha_i = 1 \tag{2}$$

Momentum conservation:

$$\begin{aligned}&\frac{\partial}{\partial t}\int_V \alpha_i \rho_i \chi \, \mathrm{v}_i dV + \oint_A \alpha_i \rho_i \chi \, \mathrm{v}_i \otimes \left(\mathrm{v}_i - \mathrm{v}_g\right)\cdot d\mathrm{a} = -\int_V \alpha_i \chi \nabla p dV + \int_V \alpha_i \rho_i \chi \, \mathrm{g} dV \\ &+ \oint_A \left[\alpha_i\left(\tau_i + \tau_i^t\right)\right]\chi \cdot d\mathrm{a} + \int_V \mathrm{M}_i \chi \, dV + \int_V \left(\mathrm{F}_{\mathrm{int}}\right)_i \chi \, dV + \int_V S_i^v \chi \, dV + \int_V \sum\left(\dot{m}_{ij}\mathrm{v}_j - \dot{m}_{ji}\mathrm{v}_i\right)\chi \, dV\end{aligned} \tag{3}$$

Energy conservation:

$$\begin{aligned}&\frac{\partial}{\partial t}\left(\alpha_i \rho_i E_i\right) + \nabla\cdot\left[\alpha_i \rho_i H_i\left(\mathrm{v}_i - \mathrm{v}_g\right)\right] + \nabla\cdot\alpha_i \mathrm{v}_g p = \nabla\cdot\left(\alpha_i k_{eff,i}\Delta T_i\right) + \nabla\cdot\left(\mathrm{T}_i\cdot\mathrm{v}_i\right) \\ &+ \mathrm{f}_i \mathrm{v}_i + \sum_{j\neq i} Q_{ij} + \sum_{(ij)} Q_i^{(ij)} + S_{u,i} + \sum_{j\neq i}\left(m_{ij} - m_{ji}\right)h_i\left(T_{ij}\right)\end{aligned} \tag{4}$$

In order to calculate the continuous and dispersed phase turbulence stresses used in Eqn. (3), the realizable k-ε turbulence model with high y+ wall treatment was employed. Details of Realizable k-ε model implemented in *STAR-CCM+* software can be found in [16]. Troshko-Hassan particle-induced turbulence

model [17] is employed as source terms to account for the bubble-induced turbulence with model coefficient, C_3, of 0.45 and damping coefficient of 1.0. The source terms for turbulent kinematic energy and dissipation are given by Eqn. (5) and Eqn. (6), respectively, as follows:

$$S_{k_c} = \frac{3}{4}\frac{C_D}{D_b}\alpha_g \rho_l \left| \mathrm{v}_l - \mathrm{v}_g \right|^3 \tag{5}$$

$$S_{\varepsilon_c} = \frac{C_3 S_{k_c}}{t_b}. \tag{6}$$

2.2 Model Description

In following sections, the details of baseline zero closure are presented. The sub-closure models not provided by STARCCM+ code have been implemented as a user-defined field functions.

2.2.1 Interfacial area density and interaction length scale

Based on the surface area of spherical particle, the interfacial area density is modeled through the use of a Sauter mean diameter d_s [18] as follows:

$$a_{ij} = 6\alpha_g / d_s . \tag{7}$$

The Sauter diameter adopts and algebraic formulation to describe the interfacial variation among different flow regimes. The Sauter mean diameter given by Eqn. (8) is implemented in *STAR-CCM+* by means of user-defined function.

$$d_s = \begin{cases} 10.06\left(p/p_0\right)^{-0.098}\sqrt{\sigma/\Delta pg}\left[\min\left(\alpha_g, 0.118\right)\right]^{0.35} & \alpha_g < 0.4 \\ 1.9425\times10^{-3}\exp\left(2.3637\alpha_g\right) & 0.4 < \alpha_g < 0.8 \\ 0.864 D_h & 0.8 < \alpha_g \end{cases} \tag{8}$$

The Yoneda correlation [19] is used for the bubbly flow regime, when α_g<0.4. An exponential trend is chosen for the intermediate flow regimes (0.4≤α_g<0.8), while the channel hydraulic diameter D_h is used as the characteristic length scale in the annular flow region (α_g≥0.8) and has a numerical constant value of 0.01278 for this application. The constant is computed as the difference between the hydraulic diameter of the sub-channel of the fuel assembly and two times the film thickness, assumed as 1.0 mm.

2.2.2 Wall heat partitioning model

In order to represent the heat transfer between the heated wall and the fluid and the boiling at the wall, a previously validate form of the classic Kurul-Podowski mechanistic heat partitioning is applied [8]. The wall heat flux consists of three components as follows:

$$\dot{q}''_w = \left(\dot{q}''_{conv} + \dot{q}''_{evap} + \dot{q}''_{quench}\right)\left(1 - K_{dry}\right) + K_{dry}\dot{q}''_{dry} . \tag{9}$$

For liquid contact with the wall, the convective heat flux is given by:

$$\dot{q}''_{conv} = \frac{\rho_l c_{pl} u_l^*}{t_l^+}\left(T_w - T_l\right). \tag{10}$$

For vapor contact with the wall, the convective heat flux is given by:

$$\dot{q}''_{dry} = \frac{\rho_g c_{pg} u_g^*}{t_g^+}\left(T_w - T_g\right) \tag{11}$$

The wall contact area fraction [16] is given by:

$$K_{dry} = \begin{cases} 0 & \alpha_\delta \le \alpha_{dry} \\ \beta^2(3-2\beta) & \alpha_{dry} < \alpha_\delta \end{cases} \tag{12}$$

$$\beta = \frac{\alpha_\delta - \alpha_{dry}}{1-\alpha_{dry}} \tag{13}$$

where α_δ is the vapor volume fraction averaged over the bubbly layer thickness and α_{dry} is the wall dryout break-point with default value of 0.9. The cell-center volume fraction is used in the dryout criterion by selecting "Wall Cell" option for specifying the bubble layer thickness.

The evaporative heat flux is determined as follows:

$$\dot{q}''_{evap} = n'' f\left(\frac{\pi d_w^3}{6}\right)\rho_g h_{lg}. \tag{14}$$

In this work, Lemmert-Chawla model [20, 21] for nucleation site number density given by Eqn.(15), Cole model [22] for bubble departure frequency given by Eqn.(16) and Tolubinsky-Kostanchuk model [23] for bubble departure diameter given by Eqn.(17) were employed to calculate the evaporative heat flux. Note that the Lemmert-Chawla nucleation site number density model and Tolubinsky-Kostanchuk bubble departure diameter model should be used together to form the effective boiling area because these correlations were tuned as one model against measured data for a wide range of conditions [12]. Lemmert-Chawla nucleation site number density is given by:

$$n'' = \left(m\Delta T_{\text{sup}}\right)^p \tag{15}$$

where m=185.0 (1/K), p=1.805 and ΔT_{sup} is the wall superheat.

Cole bubble departure frequency is given by:

$$f = \sqrt{\frac{4}{3}\frac{g(\rho_l - \rho_g)}{d_w \rho_l}}. \tag{16}$$

Tolubinsky-Kostanchuk bubble departure diameter is given by:

$$d_w = d_0 \exp\left[-\frac{\Delta T_{sub}}{\Delta T_0}\right] \tag{17}$$

where d_0 is the reference diameter with default value of 0.6 mm, ΔT_0 is the reference subcooling with default value of 45 K and ΔT_{sub} is the subcooling of the liquid. The minimum and maximum values of bubble departure diameter were specified by 0.025 mm and 1.4 mm, respectively.

The quenching heat flux is obtained by Eqn. (18) using the Del Valle Kenning model [24] for bubble induced quenching heat transfer coefficient given by Eqn. (19).

$$\dot{q}''_{quench} = h_{quench}\left(T_w - T_{quench}\right) \tag{18}$$

The quenching heat transfer coefficient is determined by the Del Valle Kenning model as follows:

$$h_{quench} = 2K_{quench} f \sqrt{\frac{\rho_l c_{pl} k_l t_w}{\pi}} \tag{19}$$

where K_{quench} is the bubble influence wall area fraction, f is the bubble departure frequency, t_w is the waiting time between the bubble departure and the nucleation of the next bubble with wait coefficient of 0.8.

The bubble influence wall area fraction is obtained using Kurul-Podowski model [9] as follows:

$$K_{quench} = C_A \frac{\pi d_w^2}{4} n'' \tag{20}$$

where C_A is the area coefficient for scaling between the nucleation site area density and the wall area fraction the bubble-induced quenching influences with the default value of 2.0.

2.2.3 Interphase momentum transfer models

The interphase momentum transfer term, $\mathbf{M}_i$, represents the sum of all the liquid-vapor interfacial forces. The interphase momentum transfer term includes contributions from the drag force, virtual mass force, lift force, turbulent dispersion force and wall lubrication force as follows:

$$\mathbf{M}_i = F_D + F_{VM} + F_L + F_{TD} + F_{WL} \tag{21}$$

where F_D is the drag force term, F_{VM} is the virtual mass force term, F_L is the lift force term, F_{TD} is the turbulent dispersion force term and F_{WL} is the wall lubrication force term.

The drag force term acting on the vapor phase due to the liquid phase is given in Eqn. (22). Tomiyama correlation [11] for a drag coefficient and the volume fraction exponent drag correction were used to calculate the drag force. Details of volume fraction exponent drag correction can be found in [16].

$$F_D = f_D C_D \frac{1}{2} \rho_l \left(\mathbf{v}_l - \mathbf{v}_g\right)\left|\mathbf{v}_l - \mathbf{v}_g\right|\left(a_{ij}/4\right) \tag{22}$$

The virtual mass force is given by Eqn. (23) with a spherical particle virtual mass coefficient, CVM, of 0.5.

$$F_{VM} = C_{VM}\rho_l\alpha_g\left(\frac{D\overline{u}_l}{Dt} - \frac{D\overline{u}_g}{Dt}\right) \tag{23}$$

The lift force term is given by Eqn. (24). While accurate lift closure are being developed, current work as evidenced the inapplicability of existing correlations [10]. The lift closure is leveraged to reproduce the key physical effect of bubble migration through a simple step function for lift coefficient given by Eqn. (25). A positive and constant value of 0.025 is used for α_g<0.25, representing almost spherical bubbles in the low void fraction regime, which accumulate near the wall; while a negative constant value of -0.025 for α_g≥0.25, representing larger wobbly bubbles that migrate towards the center of the channel.

$$F_L = C_L\rho_l\alpha_g\left(\mathrm{v}_r \times \left(\nabla \times \mathrm{v}_l\right)\right) \tag{24}$$

$$C_L = \begin{cases} 0.025 & \alpha_g \le 0.25 \\ -0.025 & 0.25 < \alpha_g \end{cases} \tag{25}$$

The turbulent dispersion force term is given by Eqn. (26) in a logarithmic form [16].

$$F_{TD} = A_D\frac{\nu_l^t}{\sigma_\alpha}\left(\nabla\ln(\alpha_l) - \nabla\ln(\alpha_g)\right) \tag{26}$$

where A_D is the mean linearized drag coefficient evaluated using a mean slip velocity and mean interfacial area, ν_c^t is the liquid phase turbulent kinematic viscosity and σ_α is the turbulent dispersion Prandtl number which was set to 1.0.

The wall lubrication force model given in Eqn. (27) is proposed by Antal et al. [25]. In this study, the wall lubrication formulation is employed with the calibration coefficients C_{w1} of -0.01 and C_{w2} of 0.05.

$$F_{WL} = -\alpha_g\rho_l\frac{\left|\mathbf{v}_g - \mathbf{v}_l\right|^2}{D_b}\max\left\{\left(C_{w1} + C_{w2}\frac{D_b}{y_w}\right), 0\right\}\mathbf{n} \tag{27}$$

2.2.4 Interphase mass transfer model

A correlation for the Nusselt number for each phase at the interface is required to model bulk boiling and condensation. Since the difference in temperature between the interface and the vapor phase is not significant, a constant value of Nusselt number for vapor phase was specified as 2.0, while Chen-Mayinger model [14] given by Eqn. (28) is employed to determine the continuous phase Nusselt number.

$$Nu_l = 0.185\,\mathrm{Re}_g^{0.7}\,\mathrm{Pr}_l^{0.5} \tag{28}$$

3. ASSESSMENT OF M-CFD APPLICABILITY

The M-CFD modeling capabilities and practicability for BWR fuel assembly were assessed against three steady-state test cases (4101-55, 4101-58 and 4101-61) of the NUPEC BFBT benchmark. The benchmark program selected these cases as validation problems for two-phase CFD modeling [6]. In these specific cases, the fuel assembly Type-4 with Ferrule-type spacers was used. Details of Ferrule-type spacer geometry can be found in [7]. The fuel bundle consists of 60 electrically-heated rods arranged in an 8×8

array, a water rod at the center of the assembly and 7 Ferrule-type spacer grids. The fuel assembly has a heated length of 3.708 m with a uniform axial power shape. The outer diameter of heater rod and rod pitch are 12.3 mm and 16.2 mm, respectively. The diameter of water rod is 34.0 mm. The inner width of channel box is 132 mm, and the corner radius of channel box is 8.0 mm. The channel flow area is 9,463 mm^2. The thicknesses of inner rings and outer rim of spacer are 0.5 mm and 1.0 mm, respectively. The height of spacer is 31.0 mm.

3.1 BFBT CFD Benchmark

3.1.1 Modeling of BFBT Full Fuel Assembly

The section describes the CFD modeling of BFBT full geometry. Major design parameters of BFBT full fuel assembly Type-4 are summarized in Table 1. Figure 1 shows the geometric configuration of the CFD model for the BFBT fuel bundle. The fuel assembly geometry has been simplified by removing dimples and springs from the original spacer geometry. Mixing tabs on the outer rim of spacer have also been removed from the model geometry. Since the Ferrule-type spacer consists of inner annuli that are in contact with each other, a line contact would exists at these locations, which is not representative of a production spacer, and would introduce challenges in the mesh discretization. In order to prevent poor quality mesh in the contact region this was modified, as shown in Fig. 1, by introducing a larger contact area. The flow area variation due to these modifications is less than 0.1 %. Figure 2 shows the mesh structure of CFD model. A hexa-dominant trimmed mesh, in combination with boundary fitted prism layers was generated with the built-in mesh generation capabilities of *STAR-CCM+* software. The mesh adopted is relatively coarse, and was selected from separate sensitivity studies. A uniform cell size of 2.0 mm is used away from the wall, while the prism boundary layer total thickness was specified to be 0.5 mm, and two layers are implemented to guarantee a $y+$ value for the near wall cell between 30 and 100. The total number of cells is 11.42 million. In this work, cell sizes less than 2.0 mm were also tested but resulted in the generation of a few low quality cells in the contact areas that created convergence issues. Further work is required in the future to address this problem in generating finer computational meshes. Figure 3 shows the cell quality metrics on two cross-sectional planes at different elevations. This cell quality metrics is based on a hybrid of the Gauss and least-squares methods for cell gradient calculation methods, which allows accounting for both the relative geometric distribution of the cell centroids of the neighbor cells, and the orientation of the cell faces. Flat cells with highly non-orthogonal faces have a low cell quality, and in two-phase flow boiling simulation have a significant influence on the stability and robustness of the simulation. Poor quality mesh in current M-CFD solvers can lead to strong local temperature over- and under-shoot and most often results in code instability. Point and line contacts in the fuel spacer region are the most common areas leading to poor quality mesh and special care should be taken to avoid having these types of geometric features. Replacing point contact or line contact in geometry with an approximated surface contact is often sufficient to improve mesh quality. The minimum mesh quality of this model was approximately 0.1 and the volume-averaged mesh quality of computational domains were 0.955.

3.1.2 Initial and Boundary Conditions

The characteristic radial power distribution inside a fuel assembly is reproduced by imposing a different heat flux, through a different multiplier, to the heating rods, as shown in Fig. 4. For instance, the heat flux of fuel rods surrounding the water rod in the central regions was specified to be 89% of the nominal heat flux of fuel rod that can be obtained by assuming the uniform radial distribution of the power. The operating conditions of three test cases were tabulated in Table 2. Inlet liquid and vapor temperatures were specified by 551.096 K and 560.538K, respectively. The operating pressure was set to approximately 7.2 MPa. The

mass flow rate was specified by 15.28 kg/s. The inlet velocity profile, turbulent kinetic energy and turbulent dissipation rate were specified to the inlet boundary as obtained from a separate fully developed single-phase flow simulation of the fuel bundle. The volume fractions of liquid and vapor at the inlet boundary were set to 0.999 and 0.001, respectively. Flow-split outlet boundary condition was specified to the outlet boundary with a split ratio of 1.0.

3.1.3 Best Practices for Solver Parameter Configuration

The appropriate configuration of the solver Under-Relaxation Factors (URFs) is of importance for the robustness and convergence of the multiphase CFD simulation. The solver URFs required for the Eulerian-Eulerian multiphase flow simulations are smaller than those for single-phase simulation. According to recommended best practices by S. Lo [26], the URFs of 0.1 for pressure and volume fraction, 0.3 for velocity, turbulence and temperature and 0.5 for other variables are recommended values for code convergence. In this study, the implicit and explicit URFs for phase coupled velocity and volume fraction were set to 0.9 and 0.1, respectively. So, the overall URFs for phase coupled velocity and volume fraction were specified to be 0.09. The URF for pressure was set to 0.1 and for other variables were set to 0.5. 2nd-order convection scheme for velocity and 1st-order convection scheme for volume fraction were employed with minimum volume fraction of zero. In this work, convergence was not reached when higher values of URFs were specified. The number of iterations required for convergence increases with lowering the values of the specified URFs. Thus, it is recommended to not use values of URFs that are excessively small.

3.2 Results and Discussion

3.2.1 Scalability Test Results

The adopted CFD model of the BFBT fuel assembly, which is comprised of 11.42 million cells, is expected to further grow with more advanced spacer designs. Therefore, the parallel performance of the CASL CFD tool represents a key to the applicability of M-CFD to full core analysis. The High Performance Computing (HPC) cluster, *Falcon*, at Idaho National Laboratory (INL) was used for all calculations. Falcon is INL's flagship cluster with over 600 TFlops of performance and 121 TB total memories. In this test, the number of iterations for the simulations was specified to be 3,000.

The most significant advantage of parallel computing is obviously the reduction in computational time. The Speedup factor (S) is used to express this reduction and it is defined as follows:

$$S(n) = t_s / t_n \tag{29}$$

where n is number of processors, t_s is the execution time on a single processor and t_n is the execution time on n-processors.

Figure 5 shows the speedup factor with increasing number of processors. The speedup factor was linearly proportional to the number of processors up to 500 processors, and while slowly reducing it still provided over 92% efficiency with 1000 cores compared with 500 cores.

Another measure to evaluate the performance of parallel computing is the cost of parallel computation (C). The cost is defined as a product of the number of processors used times the execution time as follows:

$$C = n \cdot t_n \tag{30}$$

Figure 6 shows the execution time and cost of parallel computation as a function of number of processors. The execution time of the parallel computing decreased exponentially with increasing number of processors while the cost of computation increased linearly. As for the run on a single processor, the values of cost and execution time of running a single processor were approximately 380. The execution time with 1,000 processors was significantly reduced by 0.5 hours which is 99.86% reduction compared to a single processor run, while the cost of the computation increased by 32.37% compared that of a single processor. The benefit of parallel computing in terms of cost seems not to be significant. However the execution time was dramatically reduced by the parallel computing. All execution times with a core number greater than 250 were essentially practicable for engineering applications, therefore we recommend using a number of processors between 250 and 500.

The parallelizable fraction is used to evaluate the dependency of the parallel computing efficiency on the number of processors. According to Amdahl's Law [27], the parallelizable fraction is given by:

$$\varsigma = \frac{n}{(n-1)}\left(1 - \frac{t_s}{t_n}\right) \tag{31}$$

The STAR-CCM+ software is very parallelizable so that most part of simulation was able to be parallelized as shown in Fig. 7.

3.2.2 CFD Assessment Results and Discussion

Figure 8 shows the void fraction distributions of CFD simulation and experiment. The CFD simulation results use a different color scale from the experiment to better appreciate the void distribution inside the subchannels. The average void fraction at the outlet cross section for the experiment and CFD simulations are 80.64% and 80.77%, respectively. The void fraction is higher getting far from the center of the assembly as a consequence of the radial power distribution, being higher in this region. This result shows that the M-CFD is able to qualitatively predict the concentration of the voids in the center of each subchannel. In order to quantitatively assess the accuracy of the M-CFD for BWR applications, local void fraction profiles, sub-channel averaged void fraction and exit quality are analyzed.

Figure 9 shows the lines and the sub-channel locations on the outlet boundary surface for the comparison of CFD results against experimental data. Figures 10−12 show the profiles of normalized void fraction as a function of relative distance from the center of rod bundle along different lines. The local void fraction was normalized based on the mean void fraction on each line. The baseline boiling closure model showed improved predictive capabilities for local void fraction distribution. Note that the CFD results in the literature [6] significantly underestimated the lateral void distribution while the zero closure model predicts the local void fraction profiles well. The void fractions in bulk regions of subchannel tend to be relatively higher than that in the narrow region between the heater rods. These patterns indicate as expected that the bubbles lifted off from the heated surface cluster in the bulk region of the flow. For case BFBT-4101-61 case, the local variation of void fraction distribution is relatively smaller than in the other cases. As the overall void fraction decreases, the deviation of void fraction between near-wall region and bulk region increases. In those cases with lower void fraction conditions, the interfacial forces, such as lift force, wall lubrication force, etc., would overestimate their impacts.

Figure 13 shows the computed normalized void fraction as a function of experimental void fraction. CFD results and experiments agree within a deviation of ± 20% at higher void fraction conditions (BFBT-4101-61). In this case, some data points are further away from the error boundaries and correspond to the regions near the wall. The deviation increases in the cases with lower void fraction conditions. For the BFBT-4101-58 case, it increases up to ± 30% while the BFBT-4101-55 case shows a relatively larger deviation, ranging between -50% and +35%. Results evidence that the M-CFD with the baseline zero closure model shows a great potential for BWR fuel thermal hydraulic analysis in high void fraction conditions, while accurate prediction of lower void fraction conditions will require improvement of the hydrodynamic closures for transversal forces, lift and turbulent dispersion, particularly in the transition region between wall peaked and bulk picked void distributions.

Figure 14 shows sub-channel averaged void fraction errors. These were obtained by averaging the computed local void fractions in each sub-channel. The error was calculated by subtracting the experimental sub-averaged value from the computed void fractions. In most of the sub-channels, the averaged void fraction error is less than ±10%, with a few outliers where the error remains below ±18%. The computational average void fractions of BFBT-4101-61, 4101-58 and 4101-55 were 80.77%, 62.99% and 43.79%, respectively. The corresponding experimental results were 80.64%, 63.18% and 42.75%, respectively. Computational exit qualities of BFBT-4101-61, 4101-58 and 4101-55 were 24.49%, 11.91% and 4.92%, respectively. The computational exit qualities well agree with experimental data (25%, 12% and 5%) within the relative deviation of 2%.

4. SUMMARY

A baseline boiling closure model has been implemented in the CASL CFD code, *STAR-CCM+ v11.04-010-R8*, for the BWR full fuel assembly simulation. The applicability of M-CFD for various void fraction regimes, particularly focusing on high void fraction conditions, were assessed against the international OECD/NRC BFBT benchmark data. Although simplest baseline closure model was employed, the CFD simulation results are in good agreement with experimental data in terms of local void fraction profile, subchannel void fraction and exit quality. Comparison against lower void fraction data showed the need for further improvement of the closure, where interphase momentum closure models do not appropriately capture the transition between wall-peaked and bulk-peaked distributions. As the current Best Practices of M-CFD for BWRs, it is recommended to: (1) simplify the spacer geometry in order to prevent poor mesh quality in the spacer grid regions; (2) adopt a proper mesh size avoiding low quality cells at the contact points, with boundary fitted prism layer leading to appropriately high y+ value; (3) choose appropriate solver under-relaxation factors in order to assist the convergence of simulation; (4) utilize massively parallel computation for computational feasibility with reasonable cost.

5. REFERENCES

1. A. Tentner, S. Lo, A. Ioilev, M. Samigulin and V. Ustinenko, "Computational Fluid Dynamics Modeling of Two-phase Flow in a Boiling Water Reactor Fuel Assembly," *Mathematics and Computation, Supercomputing, Reactor Physics and Nuclear and Biological Applications*, Avignon, France, Sept. 12-15 (2005).
2. A. Tentner, S. Lo, A. Ioilev, M. Samigulin, V. Ustinenko and V. Kozlov, "Advances in Computational Fluid Dynamics Modeling of Two-phase Flow in a Boiling Water Reactor Fuel Assembly," *Proceedings of the 14th International Conference on Nuclear Engineering ICONE14*, Miami, FL, July 17-20, (2006).
3. A. Tentner, S. Lo, A. Ioilev, V. Melnikov, M. Samigulin, V. Ustinenko, and S. Melinikova, "Computational fluid dynamics modeling of two-phase flow topologies in a Boiling Water Reactor fuel

assembly," *Proceedings of the 16th International Conference on Nuclear Engineering ICONE16*, Orlando, Florida, May 11-15 (2008)
4. V. Ustinenko, M. Samigulin, A. Ioilev, S. Lo, A. Tentner, A. Lychagin, A. Razin, V. Girin and Ye. Vanyukov, "Validation of CFD-BWR, a New Two-phase Computational Fluid Dynamics Model for Boiling Water Reactor Analysis," *Nuclear Engineering and Design*, **238**, pp.660-670 (2008).
5. A. Tentner, W.D. Pointer, S. Lo and A. Splawski, "Development and Validation of a Computational Fluid Dynamics Model for the Simulation of Two-phase Flow Phenomena in a Boiling Water Reactor Fuel Assembly," *Proceedings of the 17th International Conference on Nuclear Engineering ICONE18*, Brussels, Belgium, July 12-16, (2009).
6. W.K. In, D.H. Hwang and J.J. Jeong, "A Subchannel and CFD Analysis of Void Distribution for the BWR Fuel Bundle Test Benchmark," *Nuclear Engineering and Design*, **258**, pp. 211-225 (2013).
7. B. Neykov, F. Aydogan, L. Hochreiter, K. Ivanov, H. Utsuno, K. Kasahara, E. Sartori and M. Martin, "Nupec BWR Full-size Fine-mesh Bundle Test (BFBT) Benchmark, Volume I: Specification," OECD, Nuclear Energy Agency, NEA no. 6212, ISBN 92-64-01088-2 (2006).
8. E. Baglietto, M.A. Christon, "Demonstration and Assessment of Advanced Modeling Capabilities for Multiphase Flow with Sub-cooled Boiling," CASL-U-2013-0181-001, (2013).
9. N. Kurul, and M.Z. Podowski, "Multidimensional effects in sub-cooled boiling", *Proceedings of the 9th Heat Transfer Conference*, Jerusalem, Israel, Aug. 19-24 (1990).
10. R. Sugrue and E. Baglietto, "A reevaluation of the lift force in Eulerian multiphase CFD," *The 16th International Topical Meeting on Nuclear Reactor Thermal Hydraulics NURETH-16*, Chicago, Illinois, Aug.30−Sept.4 (2015).
11. A. Tomiyama, I. Kataoka, I. Zun and T. Sakaguchi, "Drag Coefficients of single bubbles under normal and micro gravity conditions", *JSME International Journal*, Series B, **41**(2), pp. 472-479 (1998).
12. S. Lo and J. Osman, "CFD Modeling of Boiling Flow in PSBT 5x5 Bundle," Hindawi Publishing Corporation, Vols. 2012, Article ID 795935, p. 8, (2012).
13. L. Schiller, and A. Naumann, "Uber die grundlegenden Berechnungen bei der Schwerkraftaufbereitung", VDI Zeits, 77(12), pp. 318 – 320, (1933).
14. Y.M. Chen and F. Mayinger, "Measurement of heat Transfer at Phase Interface of Condensing Bubble," *Int. J. Multiphase Flow*, **18**, pp. 877-890 (1992).
15. G. H. Yeoh and J. Tu, Computational Techniques for Multiphase Flows, Butterworth Heinemann, 2009.
16. Siemens PLM Software Inc., STAR-CCM+ v11.04 User Guide, (2016).
17. A.A. Troshko, and Y.A. Hassan, "A two-equation turbulence model of turbulent bubbly flows", *International Journal of Multiphase Flow*, **27**, pp. 1965-2000 (2001).
18. M. Ishii and T. Hibiki, *Thermo-Fluid Dynamics of Two-Phase Flow*, Springer, New York, USA (2006).
19. K. Yoneda, A. Yasuo and T. Okawa, "Flow structure and bubble characteristics of steam-water two-phase flow in a large-diameter pipe," *Nuclear Engineering and Design*, **217**, pp. 267-281 (2002).
20. M. Lemmert, and J.M. Chawla, "Influence of flow velocity on surface boiling heat transfer coefficient," *Heat Transfer in Boiling*, pp. 237-247 (1977).
21. M.Z. Podowski, and R.M. Podowski, "Mechanistic Multidimensional Modeling of Forced Convection Boiling Heat Transfer", *Science and Technology of Nuclear Installations*, Article ID 387020, 10 pages (2009).
22. R. Cole, "A photographic study of pool boiling in the region of the critical heat flux", *AIChE J.*, **6**, pp. 533-542 (1960).
23. V.I. Tolubinsky and D.M. Kostanchuk, "Vapour bubbles growth rate and heat transfer intensity at subcooled water boiling", *Heat Transfer* 1970, *Preprints of papers presented at the 4th International Heat Transfer Conference*, Paris, **5**, Paper No. B-2.8, (1970).
24. M.V.H. Del Valle and D.B.R. Kenning, "Subcooled flow boiling at high heat flux", *Int. J. Heat Mass Transfer*, **28**, pp. 1907-1920 (1985).
25. S.P. Antal, R.T. Lahey and J.E. Flaherty, "Analysis of phase distribution in fully developed laminar bubbly two-phase flow", *Int. J. Multiphase Flow*, **17**, pp. 635–652 (1991).

26. S. Lo, “What are the Recommended Best Practices while Troubleshooting an Eulerian Multiphase Simulation?” https://steve.cd-adapco.com/articles/en_US/FAQ/SL-5-092?type=pdf, Article number: 3519 (2015).
27. G.M. Amdahl, “Validity of the single processor approach to achieving large scale computing capabilities,” Proceedings of Am. Federation of Information Processing Societies Conf., AFIPS Press, Reston, Va., pp. 483–485, (1967).

Table 1. Geometric parameters of test assembly type 4

Parameters	Data
Simulated fuel assembly type	High Burn-up 8×8
Number of heated rods	60
Heated rod outer diameter (mm)	12.3
Heated rod pitch (mm)	16.2
Axial heated length (mm)	3708
Water rod outer diameter (mm)	34.0
Channel box inner width (mm)	132.5
Channel box corner radius (mm)	8.0
In channel flow area (mm^2)	9463
Spacer type	Ferrule
Spacer location (distance from bottom of heated length to spacer bottom face) (mm)	455, 967, 1479, 1991, 2503, 3015, 3527
Radial power shape	A (See Fig. 4)
Axial power shape	Uniform

Table 2. Test conditions for steady-state BFBT test cases [7]

Test No.	**Pressure (MPa)**	**Flow rate (t/h)**	**Inlet sub-cooling (kJ/kg)**	**Power (MW)**	**Exit Quality (%)**
4101-55	7.195	54.59	52.9	1.92	5
4101-58	7.152	54.58	50.6	3.52	12
4101-61	7.180	54.65	52.5	6.48	25

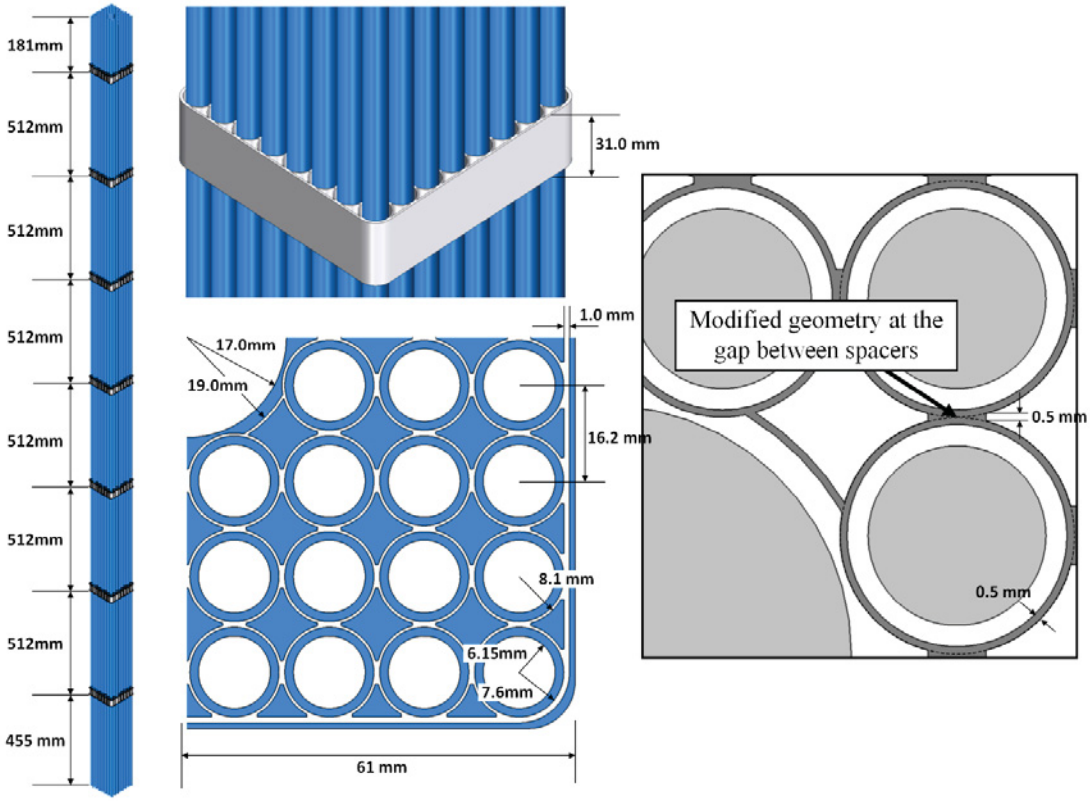

Figure 1. Computational domain of BFBT fuel bundle Type-4 with spacer grids

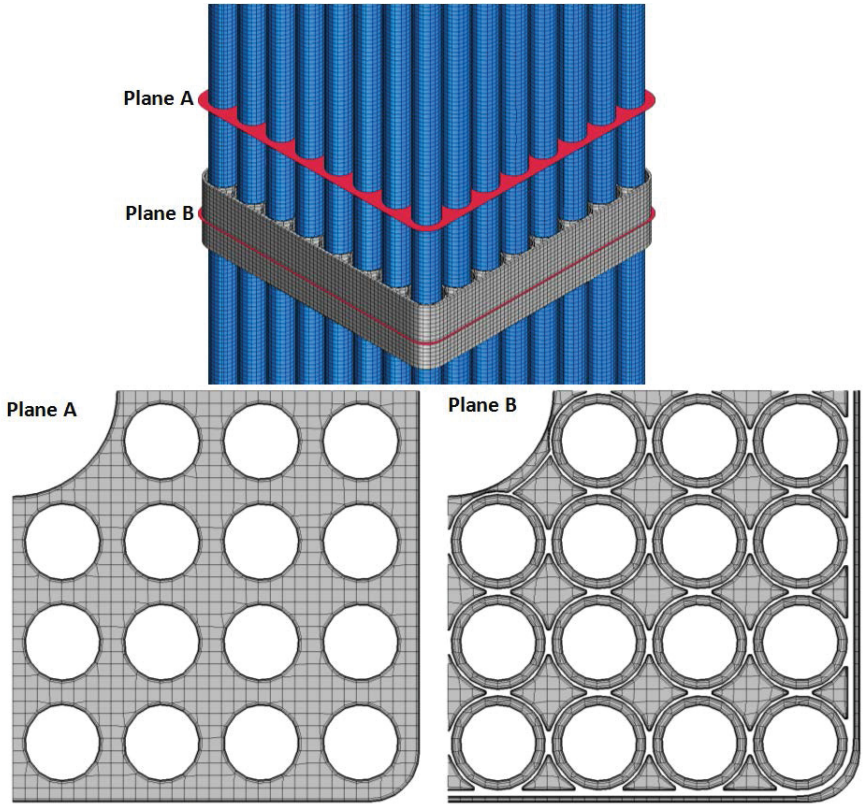

Figure 2. Mesh structure of CFD model

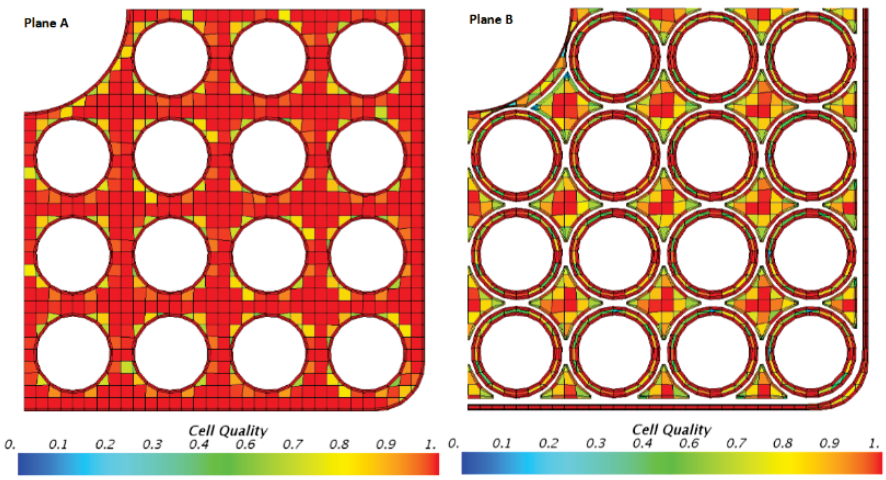

Figure 3. Mesh qualities on the cross-sectional planes of the CFD model

A (for Assembly 4, C2A, C3)

1.15	1.30	1.15	1.30	1.30	1.15	1.30	1.15
1.30	0.45	0.89	0.89	0.89	0.45	1.15	1.30
1.15	0.89	0.89	0.89	0.89	0.89	0.45	1.15
1.30	0.89	0.89			0.89	0.89	1.15
1.30	0.89	0.89			0.89	0.89	1.15
1.15	0.45	0.89	0.89	0.89	0.89	0.45	1.15
1.30	1.15	0.45	0.89	0.89	0.45	1.15	1.30
1.15	1.30	1.15	1.15	1.15	1.15	1.30	1.15

Figure 4. Radial power shape of test assembly type-4 [7]

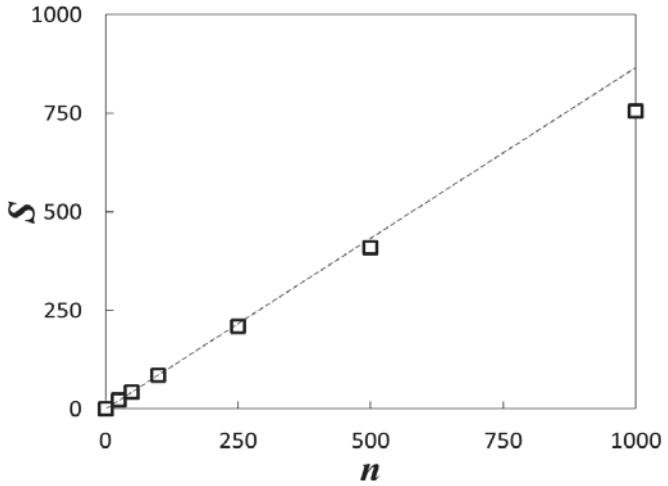

Figure 5. Plot of speedup factor as a function of number of processors

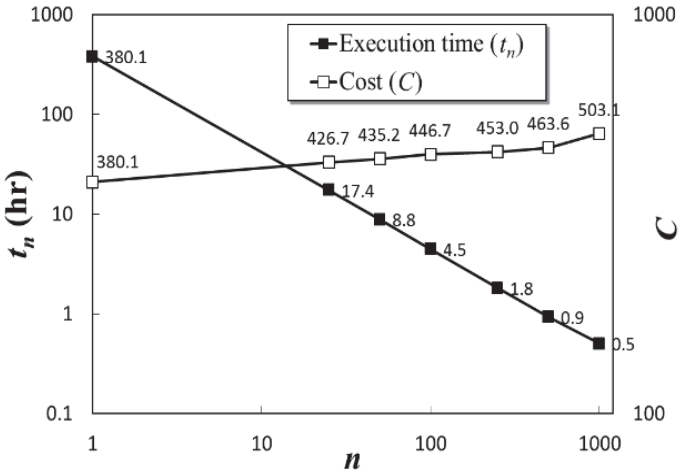

Figure 6. Plot of execution time and cost of parallel computations

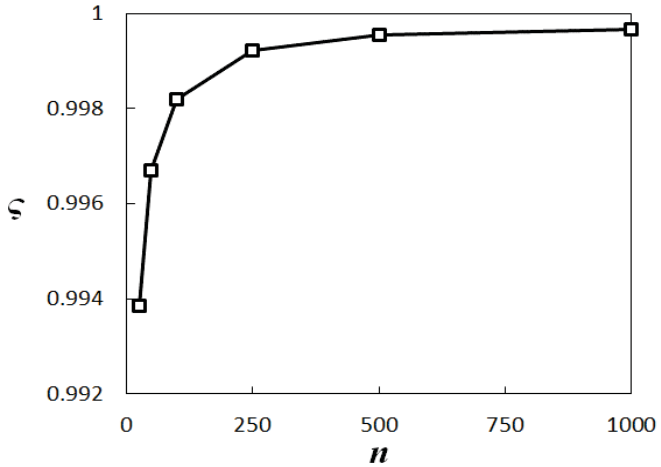

Figure 7. Plot of parallelizable fraction as a function of number of processors

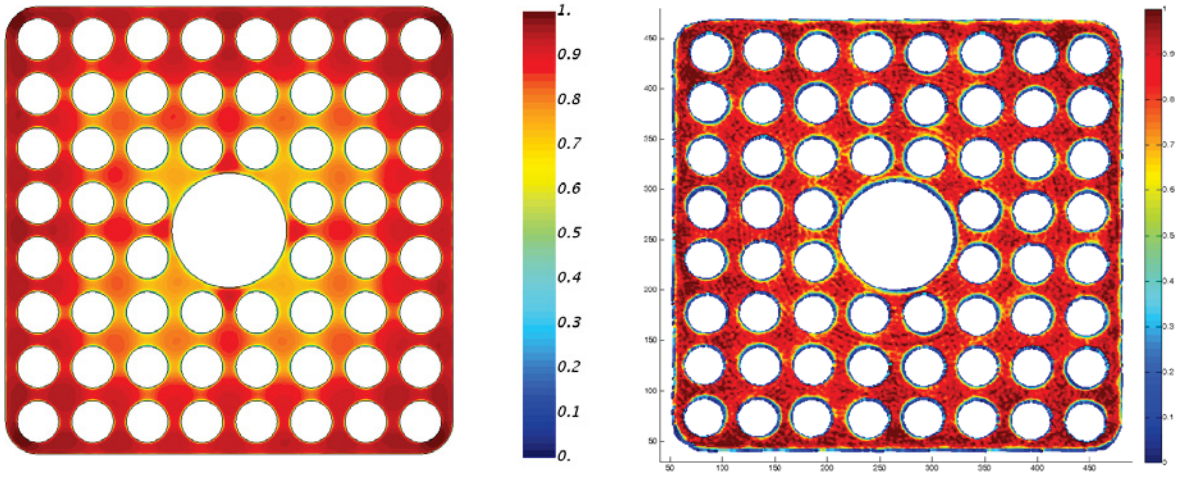

(a) CFD (α_{avg} =80.77%) (b) Experiment (α_{avg} =80.64%)

Figure 8. Comparison of void fraction distribution (BFBT 4101-61)

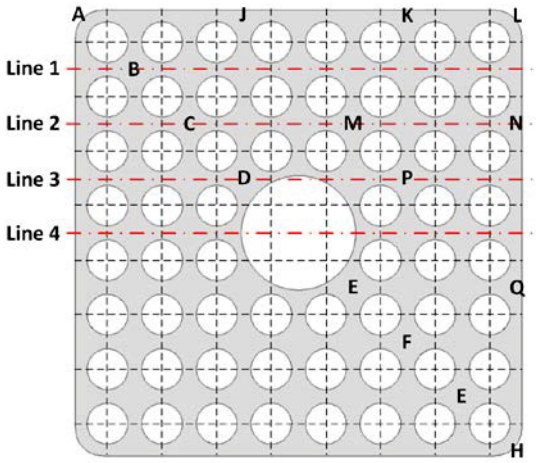

Figure 8. Reference sub-channels location

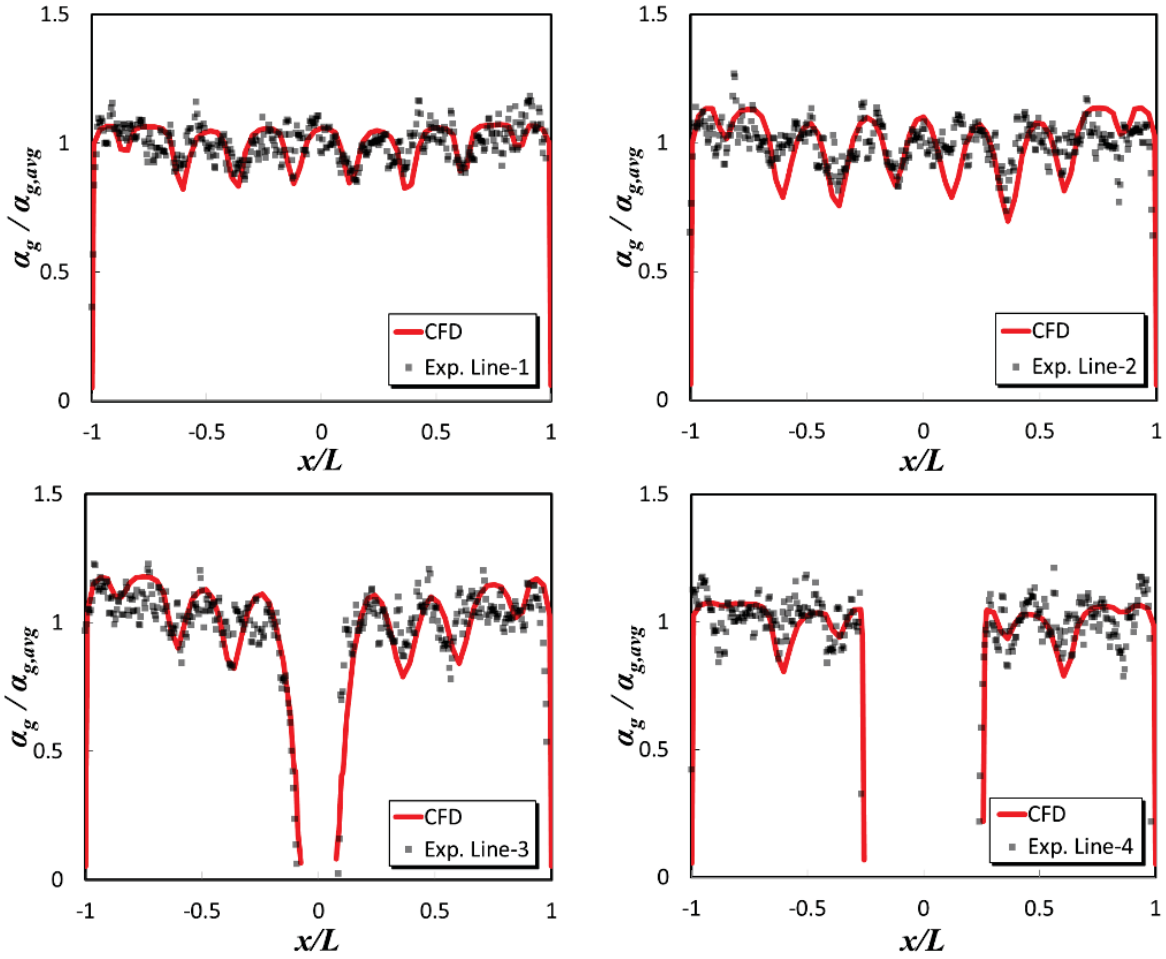

Figure 10. Normalized local void fraction profiles (BFBT 4101-61)

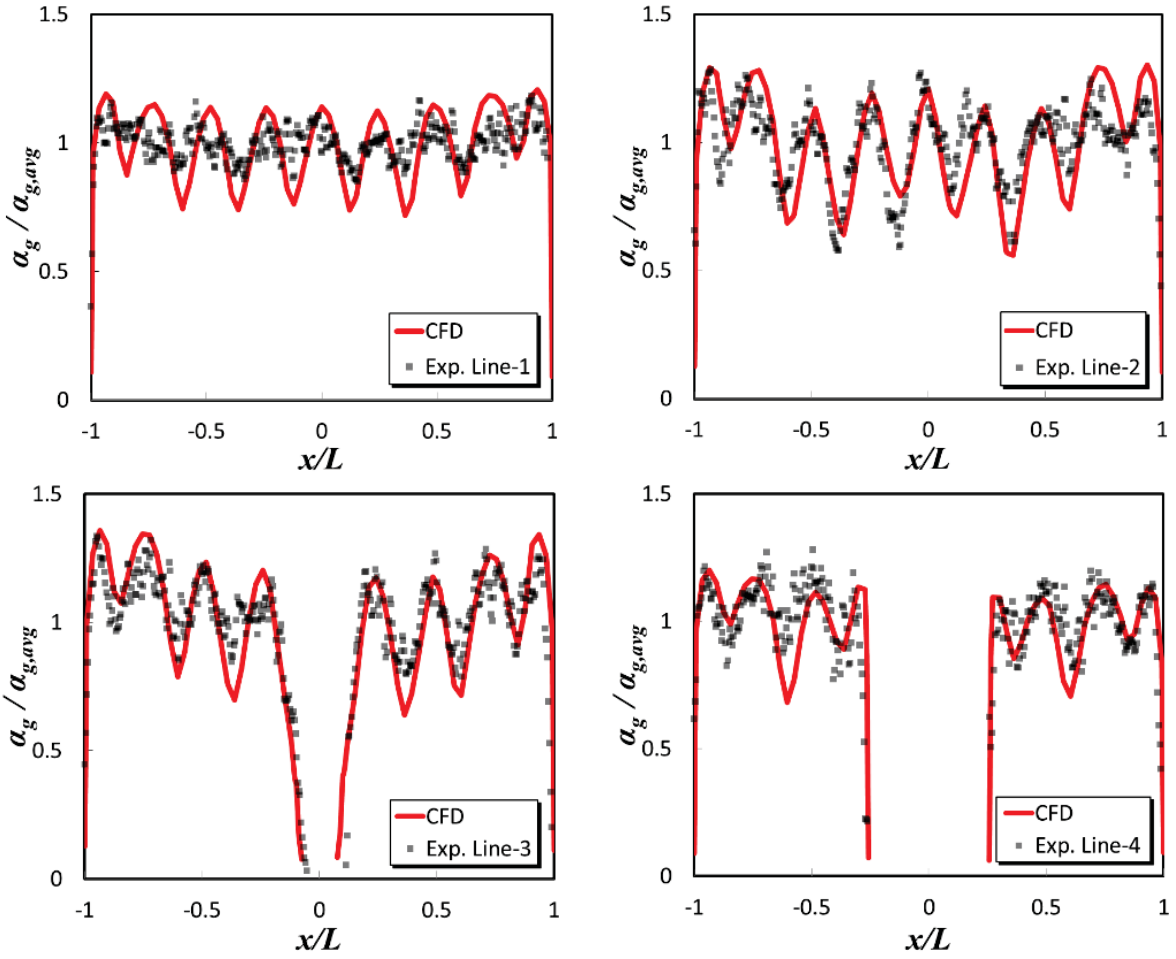

Figure 11. Normalized local void fraction profiles (BFBT 4101-58)

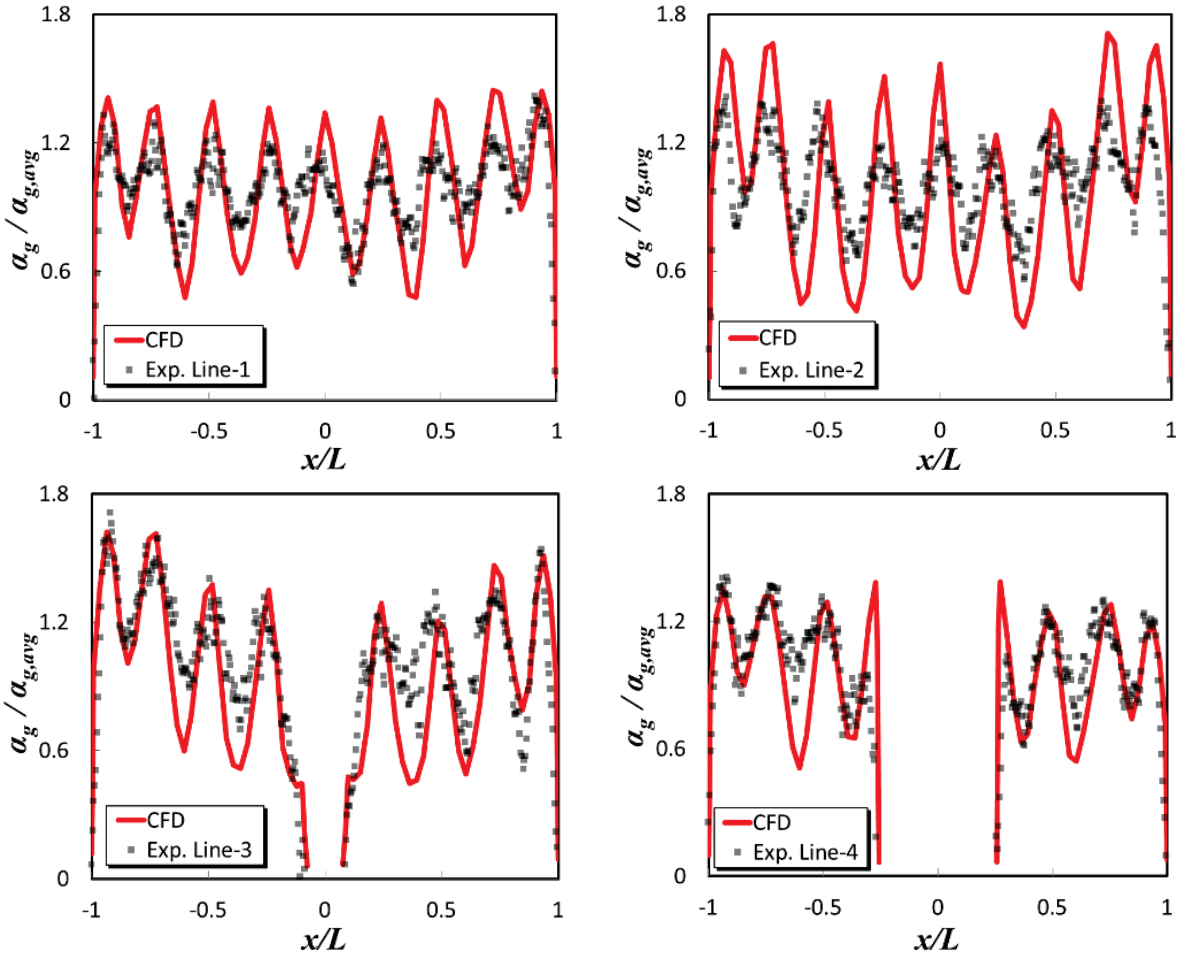

Figure 12. Normalized local void fraction profiles (BFBT 4101-55)

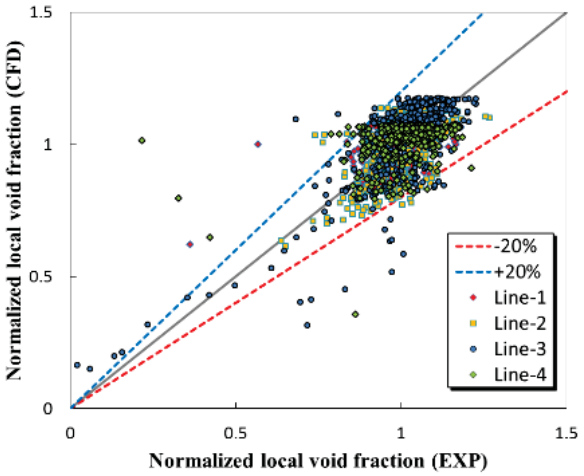

(a) BFBT-4101-61

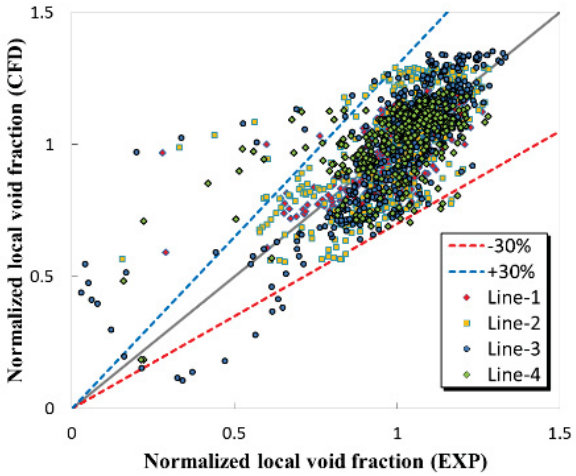

(b) BFBT-4101-58

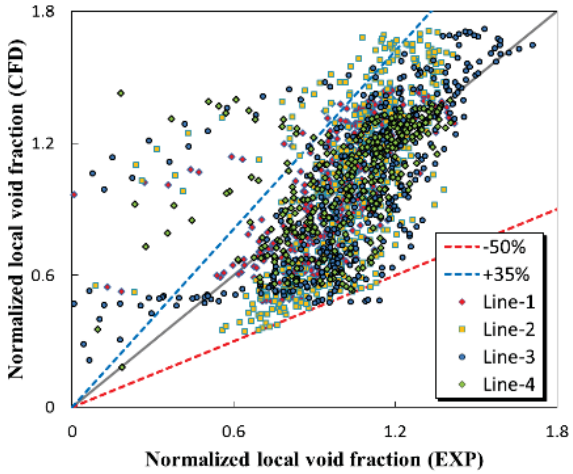

(c) BFBT-4101-55

Figure 13. Comparisons of experimental and computational normalized void fractions

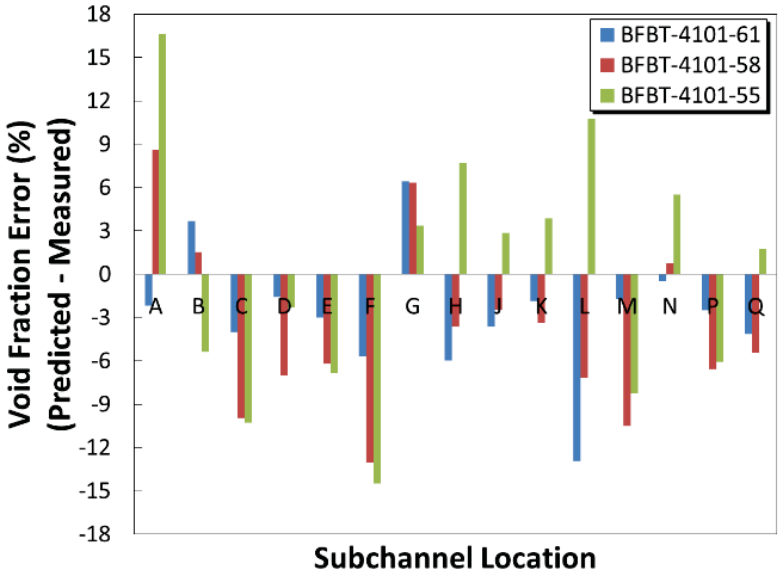

Figure 14. Subchannel-averaged void fraction error for selected subchannels